THE JOURNAL OF PHYSICAL CHEMISTRY C

ARTICLE

pubs.acs.org/JPCC

SiO_2 Aerogel Templated, Porous TiO_2 Photoanodes for Enhanced Performance in Dye-Sensitized Solar Cells Containing a Ni(III)/(IV) Bis(dicarbollide) Shuttle

Tina C. Li,[†] Francisco Fabregat-Santiago,[*,‡] Omar K. Farha,[†,∥] Alexander M. Spokoyny,[†,∥] Sonia R. Raga,[‡] Juan Bisquert,[‡] Chad A. Mirkin,[*,†,∥] Tobin J. Marks,[*,†,§] and Joseph T. Hupp[*,†,§,∥]

[†]Department of Chemistry, [§]Argonne−Northwestern Solar Energy Research Center (ANSER), and [∥]The International Institute for Nanotechnology, Northwestern University, 2145 Sheridan Road, Evanston, Illinois 60208-3113, United States

[‡]Grup de Dispositius Fotovoltaics i Optoelectrònics, Departament de Física, Universitat Jaume I, 12071, Castelló de la Plana, Spain

Supporting Information

ABSTRACT: High-area photoanodes consisting of silica aerogels, overcoated by atomic-layer-deposited TiO_2, were fabricated on transparent conducting oxide platforms for their use in dye-sensitized solar cells (DSCs) in a similar fashion as previously described. These films were characterized by scanning electron microscopy, X-ray diffraction, diffuse reflectance spectroscopy, gas adsorption, and light and dark electrochemical impedance measurements. The use of aerogel-templated photoanodes in DSCs with a Ni(III/IV) bis(dicarbollide) redox shuttle results in a greater than 2-fold enhancement in photocurrent densities, in comparison to similar cells containing photoanodes constructed from TiO_2 nanoparticles. This improvement in photocurrent is attributed to a combination of improved electron transport, increased recombination resistance across the TiO_2/electrolyte interface, and increased light scattering within the aerogel films. As a result, DSC charge collection efficiencies with this comparatively fast exchanging outer-sphere redox couple are improved in the TiO_2 aerogel templated photoanode.

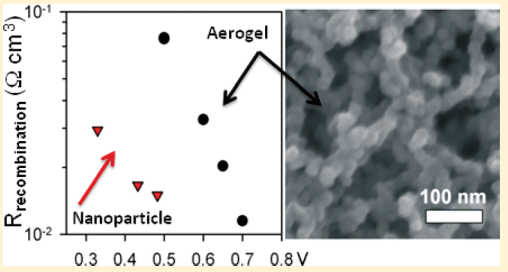

INTRODUCTION

Dye-sensitized solar cells (DSCs) have displayed significant potential to compete with silicon-based cells in the future.[1] Conventional DSCs rely on a high-surface-area, nanoparticulate TiO_2 framework, chemisorbed with a monolayer of high molar extinction dye to harvest the majority of incoming photons. O'Regan and Grätzel originally developed DSCs utilizing an iodine-containing electrolyte (I^-/I_3^- in a nitrile solvent), which efficiently regenerates a ruthenium-based polypyridyl dye and employs a platinized counter electrode which serves to reduce I_3^- back to I^-.[2] Only a handful of alternative redox shuttles have been studied to date, and of these only a select few afford DSC characteristics that approach being competitive with I^-/I_3^-.[3] It has been argued that, due to the high driving forces required for dye regeneration by I^-, the best existing DSCs perform within a percent or two of the maximum efficiency that can be achieved for I^-/I_3^- containing cells.[4] Therefore, new alternative redox shuttles with lower overpotentials for dye regeneration will need to be developed in order to realize substantially higher DSC efficiencies.[5] Additional reasons exist for seeking I^-/I_3^- alternatives[6] include the following: (a) the corrosive nature of this system, (b) the volatility of I_2, (c) specific deleterious interactions between I^- and certain ruthenium dyes, potentially leading to unproductive reaction pathways,[7] (d) direct photochemistry involving I_3^-,[8] and (e) specific deleterious interactions between I_3^- and both organic[9] and ruthenium-based dyes,[10] resulting in unproductive reaction pathways (diminished photocurrent densities) and elevated dark currents (diminished photovoltages).[11]

Recently, we reported a new metallacarborane-based redox shuttle which, when utilized in DSCs, exhibits power conversion efficiencies far superior to that of cells containing the previously studied ferrocene/ferrocenium redox couple.[12] Structurally similar to metallocenes, the Ni(III/IV) bis(dicarbollide) metallacarborane consists of two η^5-coordinated dicarbollide ligands ($C_2B_9H_{11}^{2-}$), sandwiching a nickel center (Scheme 1). Depending on whether the metal is in the formal Ni(III) or Ni(IV) oxidation state, the equatorial carbons are positioned in either a trans or cis conformation.[13] The redox-coupled structural change is important because it adds a modest kinetic barrier to the undesired reaction of the injected electron with the oxidized form of the redox couple. The barrier, in turn, slows the rate of electron interception (i.e., increases the survival time of the electron in the photoelectrode) by about 3 orders of magnitude relative to interception by ferrocenium.[12a] At the same time, the barrier is small enough to allow for fast dye regeneration. Additionally, the

Received: December 21, 2010
Revised: April 11, 2011

   dx.doi.org/10.1021/jp112139h | J. Phys. Chem. C XXXX, XXX, 000–000

Scheme 1

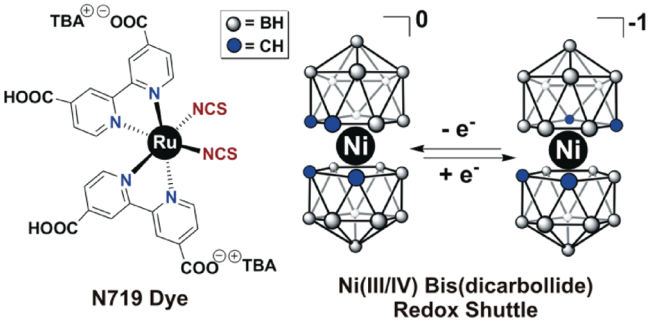

dicarbollide moiety can be easily derivatized to tune the electrochemical potential of the redox couple,[14] making this system and its congeners an attractive class of noncorrosive shuttles. Returning to interception, the rate of the reaction of Ni(IV) with the injected electron is still about 2 orders of magnitude faster than the rate for interception of the electron by I_3^-.[12a] As a consequence, charge collection in conventional nanoparticulate-based photoelectrodes is still comparatively inefficient, and overall power conversion efficiencies are still relatively low (ca. 1%), when Ni(III)/(IV) bis(dicarbollide) is used as the shuttle. Thus, additional work is needed specifically on the dynamics of the charge-collection and electron-interception processes if metallacarborane-based DSCs are to reach efficiencies similar to those of I^-/I_3^--based cells.

Here we report aerogels as a preferable framework over nanoparticles for DSCs utilizing the Ni(III/IV) bis(dicarbollide) shuttle. Alternative semiconducting frameworks have been extensively studied for DSCs with the goal of improving the optical cross sections and electron transport characteristics of these devices. Such structures have included hollow microspheres,[15] nanotubes,[16] and surface modified SiO_2 aerogels.[17] In contexts other than DCSs, aerogels have attracted attention due to their impressive strength-to-weight ratios.[18] Furthermore, since their synthesis involves a simple sol−gel process, aerogel production can be readily scaled up. More importantly, aerogel porosities and film thicknesses can be effectively controlled, with pore sizes from a few nanometers to the micrometer range, and film thicknesses controlled down to 1 μm. Thus, following facile deposition of a semiconductor via atomic layer deposition (ALD) on the SiO_2 framework, the resulting rigid aerogel films can be used as DSC photoanodes. Through ALD, a large variety of metal oxides (e.g., ZnO, ZrO_2, SnO_2)[19] can be conformally coated on the rough aerogel surface, making this porous structure applicable to many types of solar cells.

EXPERIMENTAL SECTION

Solar Cell Fabrication. Aerogel films were prepared by similar methods as previously reported,[20] but with different silica and base concentrations and alcogel aging conditions. The modified conditions yield aerogels that are somewhat more porous and of lower density than those studied in the earlier report. Briefly, a prehydrolyzed ethyl polysilicate solution (Silbond Corp.) was diluted to 33% by volume with ethanol and mixed in a 1:1 ratio with the base catalyst solution (1.7 mL of 30% NH_4OH, 40 mL of ethanol, 50 mL of H_2O). In a vapor-saturated chamber of 1:1 ethanol:water, 6 − 10 μL of the silica solution was drop cast onto the fluorine-doped tin oxide substrates (TEC8 FTO, Hartford Glass) to form smooth alcogel films. These films were allowed to age overnight and were repeatedly solvent exchanged with anhydrous ethanol, and finally with liquid CO_2, which is then removed under supercritical conditions. Supercritical drying is crucial as it eliminates solvent capillary effects that would otherwise collapse the aerogel. The active areas of the aerogels (~0.2 cm^2) were then defined by quickly scraping the films with a razor blade. The aerogel substrates were transferred to an ALD reactor (Savannah 100 ALD instrument, Cambridge Nanotech, Inc.) for TiO_2 growth at 200 °C. Alternating pulses of titanium isopropoxide (TIPS, Aldrich) and Milli-Q H_2O were used, with pulse times of 0.5 and 0.03 s, respectively, and exposure times of 4 s for each reactant. The amorphous TiO_2-coated aerogels were then heated at 500 °C for 30 min (to convert the semiconductor to its anatase form), cooled to 80 °C, and dye loaded in a 3.0×10^{-4} M solution of *cis*-bis(isothiocyanato)bis(2,2′-bipyridyl-4,4′-dicarboxylato)ruthenium(II) bis(tetrabutylammonium) (N719, Dyesol) in CH_3CN:*tert*-butyl alcohol (50:50 vol %) for 24 h. The substrates were then rinsed with acetonitrile and dried under N_2. Alternatively, TiO_2 nanoparticle photoanodes were prepared as previously reported.[12a] Briefly, commercial paste (Dyesol 18NR-T) was doctor bladed onto FTO with an 11 nm TiO_2 blocking layer formed by ALD, sintered at 500 °C, and cooled to 80 °C prior to dye loading. For Al_2O_3 ALD, deposition was carried out at a reactor temperature of 200 °C, with alternating pulses of trimethylaluminum (TMA, Aldrich) and Milli-Q H_2O and pulse times of 0.02 and 0.03 s, respectively. Dye-sensitized photoanodes were sandwiched to predrilled platinized FTO (TEC15 FTO, Hartford Glass), melting the thermoplastic spacer (Surlyn-30, Dyesol) at 80 °C on a hot plate. The electrolyte solution, consisting of 0.030 M $[NMe_4]$−Ni(III) bis(dicarbollide), 1.8×10^{-3} M Ni(IV) bis(dicarbollide), 6.0×10^{-3} M $[NMe_4]BF_4$, and 0.036 M 4-*tert*-butylpyridine in 85:15 acetonitrile:valeronitrile, was introduced into the cell by backfilling with a vacuum and sealed with a Suryln thermoplastic film and cover glass slide.

For DSCs with I^-/I_3^-, the electrolyte was prepared using 0.6 M 1-butyl-3-methylimidazolium iodide, 0.03 M I_2, 0.1 M guanidinium thiocyanate, and 0.5 M 4-*tert*-butyl pyridine in acetonitrile:valeronitrile (85:15).

Solar Cell Characterization. Film thicknesses were determined by profilometry (Tencor P10), and scanning electron microscopy was performed using a scanning electron microscope (Hitachi S-4800-II cFEG SEM). Powder X-ray diffraction (PXRD) patterns were recorded with a Rigaku XDS 2000 diffractometer using Ni-filtered Cu Kα radiation and used to examine the TiO_2 phase composition, scanning in 0.1 step increments at 3 s/step. Samples for diffuse reflectance were prepared on microscope cover glass and performed with a Cary 5000 spectrophotometer equipped with a Varion External DRA-2500 accessory.

Nitrogen adsorption isotherms were measured on bulk aerogel samples with an Autosorb 1-MP and Quadrasorb SI from Quantachrome Instruments. These samples were activated at 120 °C for 5 h under vacuum prior to measuring isotherms. Ultrahigh purity grade nitrogen was used for all adsorption measurements. Specific surface areas were calculated using the Brunauer−Emmett−Teller (BET) method, the mesopore size distributions were calculated from the desorption branch by the Barrett−Joyner−Halenda (BJH) method, and the micropore size distributions were calculated by the Saito−Foley (SF) method. Surface areas of electrode-supported aerogel films were measured via krypton adsorption (see Supporting Information, Figure S1).

dx.doi.org/10.1021/jp112139h |*J. Phys. Chem. C* XXXX, XXX, 000–000

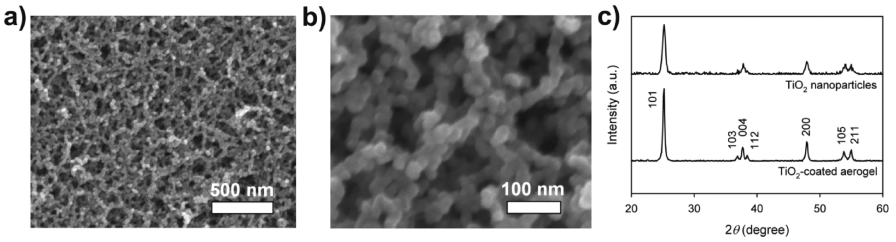

Figure 1. (a, b) Typical SEM images of aerogels coated with ~10.5 nm of TiO_2. (c) X-ray diffraction patterns for 7 μm thick TiO_2 nanoparticle and aerogel films.

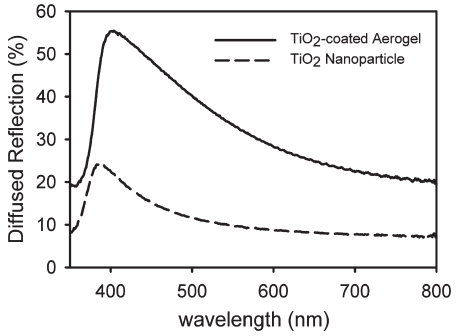

Figure 2. Diffuse reflectance comparison of 7 μm thick TiO_2-coated SiO_2 aerogel and TiO_2 nanoparticle films in air. (Scattering is anticipated to be less for solvent-infiltrated films.) While both consist of particles of ca. 20 nm width, the aerogel fibrils additionally define features having dimensions of a few hundred nanometers. The enhanced scattering by the aerogel film is ascribed to these larger structures.

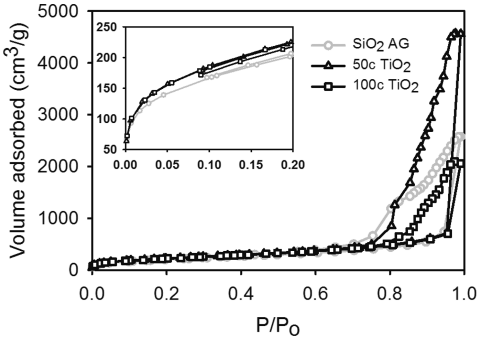

Figure 3. N_2 isotherms of pure SiO_2 aerogel ("SiO_2 AG"), SiO_2 AG with 50 ALD cycles of TiO_2 ("50c TiO_2"), and SiO_2 AG with 100 ALD cycles of TiO_2 ("100c TiO_2"). The inset shows the low pressure region.

Photovoltaic characteristics were measured under AM 1.5 conditions, using a solar simulator (Spectra-Nova Technologies), with the Xe lamp calibrated to a KG3 filter. Incident-photon-to-current conversion efficiencies (IPCEs) were measured using a monochromator (Jobin-Yvon fluorescence spectrometer) and a potentiostat (CH Instruments 1202). Impedance measurements were performed with a Solartron 1260A frequency response analyzer coupled to a Solartron 1286 electrochemical interface, using a two-electrode configuration. DSCs were polarized over a potential range of 100−650 mV in 50 mV increments for dark electrochemical impedance spectroscopic (EIS) analysis and in a range of ±100 mV around the open-circuit potential (OCP) for light EIS analysis under 100 mW/cm^2 illumination, with a 10 mV ac perturbation and swept over a frequency range of 30 mHz−300 kHz.

RESULTS AND DISCUSSION

TiO_2−Coated SiO_2 Aerogels. TiO_2-coated SiO_2 aerogel thin films resemble a network of strings of beads (Figure 1), with the SiO_2/TiO_2 core−shell particle radii primarily determined by the TiO_2 deposition thickness. Powder X-ray diffraction confirms the presence of polycrystalline anatase in the ALD-derived TiO_2, with characteristic Bragg reflections identical to those of the nanocrystalline TiO_2 particles. Although the aerogel and nanoparticulate films have similar *particle* feature sizes (ca. 20 nm), the former are substantially better light scatterers; see the diffuse reflectance spectra in Figure 2. The basis for the enhanced scattering by the aerogel is the presence of macropores a few hundred nanometers wide. Importantly, the macropores are retained when TiO_2 is deposited. These macropores are clearly evident in scanning electron micrographs (Figure 1b). Additionally important for achieving strong light scattering is a high degree of refractive index contrast between the aerogel and the electrolyte solution. ALD of TiO_2 substantially increases the average refractive index of the aerogel structure and, therefore, the refractive index contrast. Scattering could advantageously increase light absorption in the DSC. However, depositing excess semiconductor could conceivably compromise film porosity, depending on the parent SiO_x sol−gel composition used, and hence the SiO_2 aerogel porosity. To quantitatively evaluate the microporosity and mesoporosity associated with the aerogels, volumetric N_2 adsorption experiments were conducted.

Isotherms obtained using N_2 as an adsorbate on bulk aerogel samples reveal typical type II isotherms (Figure 3) consistent with the observed morphology of the thin films prepared under identical conditions as for the SEM studies. Indeed, the isotherms display components characteristic of both microporosity (sharp uptake of N_2 at pressures below 0.2 atm) and mesoporosity (hysteresis loop at higher pressure), where adsorbent−adsorbate interactions are weakened.[21] The observed microporosity is a structural consequence of morphological features possessed by SiO_2 and/or by the TiO_2 on the aerogel's interior surface. Figure 4a shows that the micropores have widths centered around ~1.5 nm. The micropores provide the bulk aerogels with high surface areas. For aerogel films, the micropores provide sizable roughness factors, i.e., values similar to those for nanoparticle films of the same thickness. As shown in the Supporting Information (direct surface area measurements on aerogel films using Kr as an adsorbate), aerogel roughness factors per unit length are over 100 per μm of film thickness. Pore size distributions are similar for SiO_2 and TiO_2@SiO_2 aerogels, implying that semiconductor deposition is conformal. With heat treatment at 500 °C, not only is the crystallinity of the TiO_2

dx.doi.org/10.1021/jp112139h |J. Phys. Chem. C XXXX, XXX, 000–000

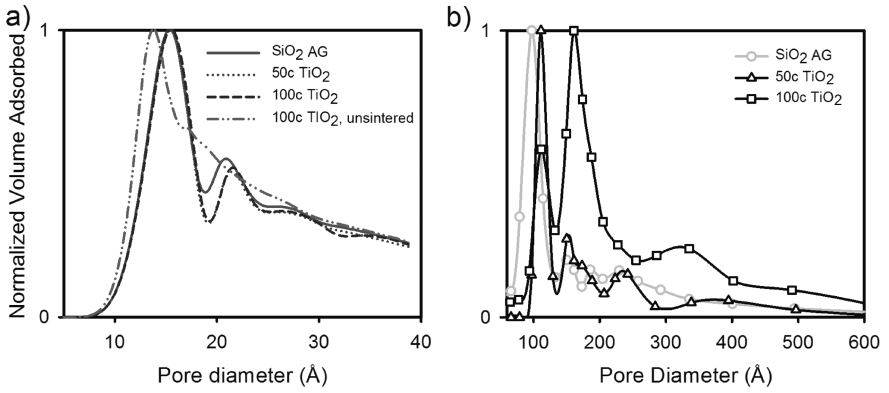

Figure 4. Normalized (a) micropore and (b) mesopore size distributions of various bulk aerogel samples prepared in this study.

Table 1. Surface Areas of Bulk SiO_2 Aerogel Samples with 0, 50, and 100 Cycles of ALD-Deposited TiO_2

sample	SiO_2 aerogel treatment	amt (radial thickness) of TiO_2 deposited (nm)	surface area (m^2/g)
SiO_2 AG	with no ALD, not heated	0	698
50c TiO_2	with 50 ALD cycles, heated	1.8	757
100c TiO_2	with 100 ALD cycles, heated	3.5	767

coating increased, but the pore size distribution becomes more well-defined. As expected, Brunauer−Emmett−Teller (BET) surface areas (Table 1) increased slightly as increasing amounts of TiO_2 were deposited on the aerogels. Surface areas for coated aerogels averaged ~760 m^2/g. Photoanodes were prepared in the same manner.

Photovoltaic Performance of Ni(III)/(IV) Bis(dicarbollide) DSCs with Aerogel-Templated Photoanodes. Utilizing the aforementioned SiO_2 aerogel frameworks, we observe enhancements in short-circuit current densities (J_{sc}) from 2.4 mA/cm^2 in nanoparticles to over 6 mA/cm^2 in aerogels (Figure 5). As a result, DSC performances are significantly improved, achieving power conversion efficiencies of over 2% for this Ni(III)/(IV) shuttle, compared to 0.8% with a TiO_2 nanoparticulate photoanode. This improvement is also reflected in the incident-photon-to-current conversion efficiencies shown in Figure 5a. Dye desorption experiments indicate that the extent of dye loading is similar for the aerogel and nanoparticle samples, consistent with the similarity of roughness factors for the two types of electrodes. Neglecting light-scattering effects (for simplicity, and because we are not able to quantify their contributions), the light-harvesting efficiencies (N719) of the aerogel and nanoparticle films are essentially identical. Expressed another way, the apparent *absorbed*-photon-to-current conversion efficiencies (APCE curves) are more than twice as large for aerogel electrodes compared with nanoparticle films (both 8 μm thick). Note that, in reality, the greater light scattering by the aerogel electrode likely accounts for a significant fraction of the observed enhancement in photocurrent densities.

Unlike the majority of cobalt-based redox shuttles studied, the present Ni(IV) bis(dicarbollide) does not suffer from significant mass transport issues.[12a] Thus, for devices incorporating either the TiO_2 nanoparticle or the aerogel electrodes, the magnitude of J_{sc} is linearly correlated with illumination intensities up to at least

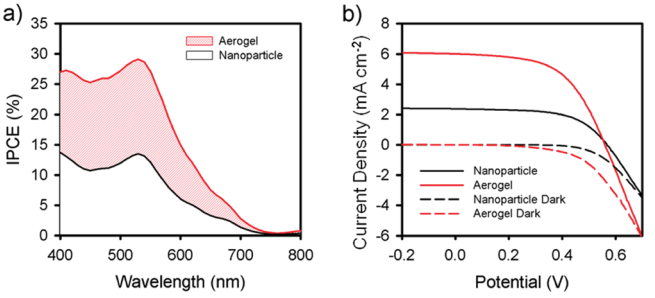

Figure 5. Comparison of Ni(III)/(IV) bis(dicarbollide) DSCs fabricated with 8 μm thick SiO_2 aerogel film coated with 10.5 nm of TiO_2 and 8 μm thick nanoparticulate film consisting of ~20 nm diameter TiO_2 particles: (a) incident-photon-to-current conversion efficiencies and (b) $J-V$ characteristics.

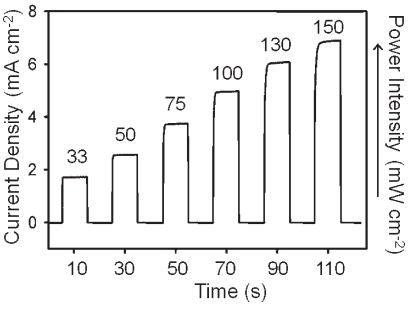

Figure 6. Current generated by a Ni(III)/(IV) bis(dicarbollide) DSC with an aerogel framework at various illumination intensities (as specified by inset) as a function of time.

1 sun. However, from transient short-circuit measurements (see Figure 6), where aerogel DSC behavior for light intensities up to 1.5 suns (150 mW/cm^2) was monitored in 10 s intervals, the current generated at light intensities above 1 sun requires a few seconds to reach its maximum (i.e., steady-state) value. This is the opposite of what one would expect if the photocurrent density were limited by the rate of diffusion of Ni(IV) to the dark electrode (i.e., steady-state J_{sc} values would be lower than initial values). In any case, the transient behavior does not appear to adversely affect overall device performances above intensities of 1 sun. For example, for a DSC utilizing a 8.0 μm thick aerogel photoanode, at an illumination intensity of 150 mW/cm^2 (about

dx.doi.org/10.1021/jp112139h |J. Phys. Chem. C XXXX, XXX, 000–000

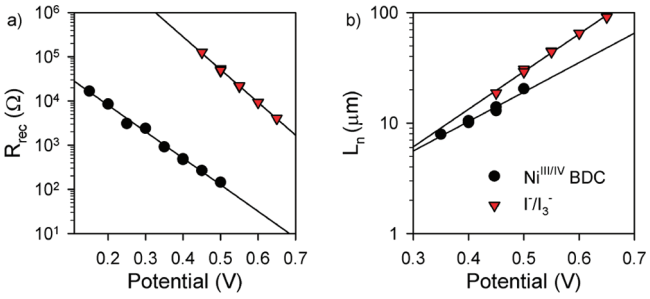

Figure 7. Potential dependence of (a) charge recombination resistance R_{rec} and (b) diffusion length L_n for Ni(III)/(IV) bis(dicarbollide) and I^-/I_3^- DSCs. Both types of cells featured a 10 μm thick TiO_2−SiO_2 aerogel framework with no Al_2O_3 deposition. The lower values of R_{rec} and L_n obtained for Ni(III)/(IV) bis(dicarbollide) DSCs limit the charge collection efficiency, yielding a lower short-circuit current density and a smaller optimal thickness for the aerogel film.

1.5 suns) the power conversion efficiency remains close to 2%. Thus, the porous aerogel structure ensures good permeation by, and diffusion of, redox-active electrolytes such as the prolate spheroid shaped[22] Ni-based metallacarborane shuttle and its countercation. We suggest that the aerogel architecture could alleviate mass transport issues with bulkier DSC redox shuttles—a point we are investigating separately.

Electrochemical Impedance Spectroscopy. To investigate the various kinetic processes occurring across the multiple interfaces in the TiO_2-nanoparticle-based and aerogel-based DSCs, electrochemical impedance spectroscopy (EIS) was utilized. With the proper model, steady-state DSC characteristics such as electron transport resistance through the TiO_2 network R_{tr}, recombination resistance at the TiO_2/electrolyte interface R_{rec}, and the TiO_2 chemical capacitance C_μ, can be extracted from the frequency-dependent response to a small perturbation in the external electrical potential as a function of the average applied bias voltage. Bisquert et al. have developed a physically relevant transmission line model for DSCs utilizing the I^-/I_3^- redox shuttle to derive these parameters.[23] Thus, values for the electron diffusion coefficient $D_n = L^2(R_{tr}C_\mu)^{-1}$, lifetime in the photoelectrode $\tau_n = R_{rec}C_\mu$, and effective diffusion length $L_n = L(R_{rec}/R_{tr})^{1/2} = (D_n\tau_n)^{1/2}$ can be calculated to evaluate DSC performance. Applying the same transmission line model to DSCs utilizing the Ni(III)/(IV) bis(dicarbollide) redox shuttle, the overall recombination resistance R_{rec} (i.e., resistance associated with interception of injected electrons by the oxidized shuttle) was determined to be $\sim 10^2$ smaller for Ni(IV) bis(dicarbollide) than for I_3^- (Figure 7). Comparable results were obtained from the open-circuit voltage (V_{oc}) decay technique, where interception rates of injected electrons by Ni(IV) bis(dicarbollide) are 10^2 times faster than those by I_3^-,[24] largely accounting for the lower V_{oc} values found for cells containing the nickel-based shuttle.[4] Consequently, apparent diffusion lengths are noticeably shorter with the metallacarborane system.

Here the impedance experiments were performed in the dark with DSCs containing a 10 μm thick TiO_2-coated SiO_2 aerogel photoanode, with the resulting L_n obtained in the presence of Ni(III)/(IV) bis(dicarbollide) being approximately half the ratio obtained in the presence of I^-/I_3^-, at potentials near their respective V_{oc} values, as shown in Figure 7b.

EIS measurements made under illumination can provide additional physical elements relevant to DSC performance under

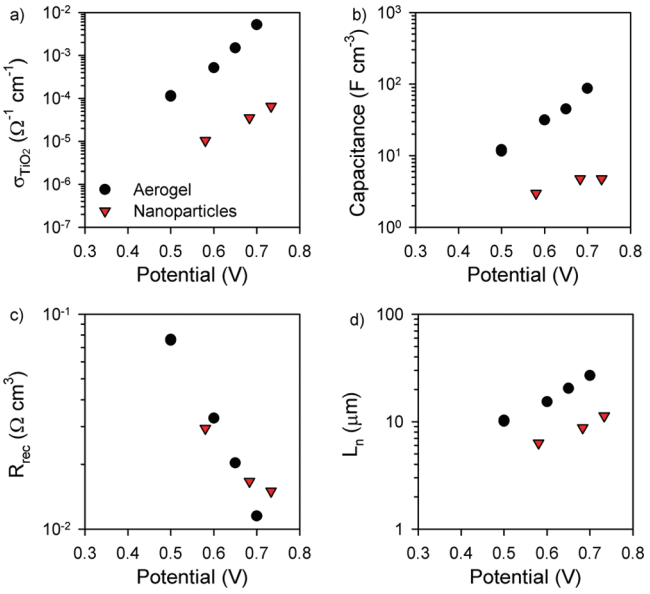

Figure 8. Impedance spectroscopy results for an ALD-deposited TiO_2@SiO_2 aerogel compared to a TiO_2 nanoparticle framework with one ALD cycle of Al_2O_3 using the Ni(III)/(IV) bis(dicarbollide) electrolyte. (a) TiO_2 electronic conductivities, (b) film capacitances normalized to volume, (c) charge recombination resistances normalized to volume, and (d) diffusion lengths (charge-collection distance) for working DSCs.

operating conditions (Figure 8). For example, the electron conductivity within the dye-illuminated TiO_2 can be calculated from R_{tr} using the following relationship:

$$\sigma_n = \frac{L}{A(1-p)R_{tr}} \quad (1)$$

where L is the photoanode length, A is the area of the film, and p is its porosity ($p \sim 0.95$ for the aerogel while $p \sim 0.60$ for the nanoparticle). Assuming that the mobility (μ) is constant, the conductivity ($\sigma = q\mu n$; where q is the electron charge) is exclusively dependent on the number of free electrons in the conduction band, yielding

$$\sigma_n = \sigma_0 \exp\left[\frac{E_{Fn} - E_C}{k_B T}\right] \quad (2)$$

In eq 2, σ_0 is a constant, k_B is the Boltzmann constant, T is the temperature, E_{Fn} is the quasi-Fermi level of electrons in the semiconductor, and E_C is the conduction band edge energy. A rise in the conduction band edge will displace the conductivity toward higher potentials as $V = (E_{redox} - E_{Fn})/q$. Here, data extracted from the impedance analysis reveal higher electron conductivities through the aerogel films (Figure 8a), indicating faster charge collection through these devices. Note that, in our experiments, the values of series resistance and current are small enough to allow the corresponding potential drop to be neglected; thus the applied potential needs no further correction.

The normalized chemical capacitance for the TiO_2 electrode is given by

$$C_\mu^{norm} = \frac{C_\mu}{LA(1-p)} \quad (3)$$

where C_μ is the measured chemical capacitance and the film

dx.doi.org/10.1021/jp112139h |J. Phys. Chem. C XXXX, XXX, 000–000

thickness L, area A, and porosity p determine the semiconductor volume. Normalization enables the capacitances for photoelectrodes of differing thickness or differing architecture (i.e., nanoparticle vs aerogel) to be meaningfully compared.

The chemical capacitance provides information about of the density of electronic states (DOS) below the conduction band. Assuming that these states represent the tail of the Boltzmann distribution, it follows that[25]

$$C_\mu = \frac{N_L q^2}{k_B T} \exp[-\alpha(E_C - E_{Fn})/k_B T] \quad (4)$$

where N_L is the total number of electron trap states below the conduction band and α is a factor that describes the distribution of these states, generally known as traps.

The charge-transfer resistance arising at the porous nanostructured electrode in contact with liquid electrolyte may be described by using a recombination resistance (or charge-transfer resistance), R_{rec}, that varies with the Fermi level as

$$R_{rec} = R_0 \exp\left[\beta \frac{E_{redox} - E_{Fn}}{k_B T}\right] \quad (5)$$

In eq 5, R_0 is a constant indicating the onset of recombination, and β is the recombination coefficient, a factor governing the charge-transfer losses from TiO_2 to the Ni(III)/(IV) bis(dicarbollide) redox. As the architectures present similar roughness factors (see the Supporting Information), the normalization may be done by assuming that recombination losses are proportional to the film volume:

$$R_{rec}^{norm} = R_{rec} LA \quad (6)$$

From Figure 8c, we obtain similar values for the resistance around V_{oc}, but different slopes. Thus, in the aerogel $\beta = 0.23$, while in the nanoparticle architecture $\beta = 0.13$. These values are half the values typically found in the case of TiO_2 nanoparticles and I^-/I_3^-.[26] The values of β determine the maximum fill factor (FF) attainable by the solar cell.[27] The difference in β values appears to explain why the FFs for aerogel DSCs are greater than the FFs for nanoparticle DSCs, despite the greater series resistances of the former (35 vs 19 Ω).

The sizable data displacements in Figure 8a,b suggest a higher conduction band edge energy for the nanoparticle electrodes relative to the aerogel electrodes (see eqs 2 and 4). Chemically meaningful comparisons of certain impedance parameters, such as R_{rec}, require that values for $E_C - E_{Fn}$ for different kinds of photoelectrodes be similar. One approach to correcting for possible differences in the quantity $E_C - E_{Fn}$ is to assume that the electrodes contain identical numbers of electrons per unit volume at the same potential relative to E_C.[28] For a given impedance data set, this condition is satisfied by representing the data as electron conductivity and displacing the sample data set potential by the difference in conduction band edge energy, ΔE_C, relative to a reference sample.[29,30] Therefore we use the potential

$$V_{ecb} = V - \Delta E_C/q \quad (7)$$

where "ecb" stands for "common equivalent conduction band." By simultaneously aligning the conductivity and capacitance data sets, electron mobilities are made equivalent in comparisons of the two samples. Using this approach (Figure 9), we obtain a change in the conduction band $\Delta E_C \approx 0.25$ V.

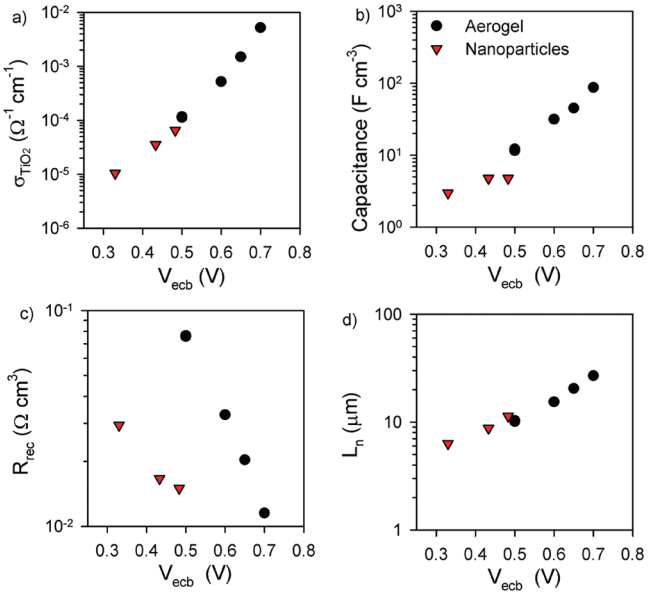

Figure 9. Comparison of impedance spectroscopy data of Figure 8 with respect to the common equivalent conduction band potential obtained after displacing the TiO_2 nanoparticle data by −0.25 V. (a) TiO_2 electronic conductivities, (b) film capacitances normalized to volume, (c) charge recombination resistances normalized to volume, and (d) diffusion lengths (charge-collection distance) for working DSCs.

This displacement-based adjustment has interesting consequences. Plots of recombination resistance versus "corrected" potential are now significantly shifted such that the nanoparticle-based electrode exhibits recombination times that are roughly an order of magnitude shorter than those of the aerogel electrode (for a given potential, relative to the appropriate conduction band edge energy). This conclusion, if correct, suggests that the nanoparticulate electrode (relative to the aerogel electrode) may possess a greater number of sub-band-edge states capable of mediating electron recombination.[31]

From the EIS analysis under illumination, L_n can be calculated and is observed to rise smoothly with potential for both the aerogel and nanoparticle DSCs, as reported previously (for nanoparticle DSCs).[32] The apparent charge-collection distance (L_n) for the aerogel DSC is relatively large, extending toward 20 μm at V_{oc}, following the tendency marked by the nanoparticles as shown in Figure 9d. Note, however, that L_n values derived via this technique constitute a small perturbation diffusion length.[33]

If ALD-deposited TiO_2 aerogel photoanodes with 6 μm thickness are employed in a Ni(III)/(IV) bis(dicarbollide) based DSC, the charge-collection efficiency should be close to unity (since $L_n/L > 1$ at the maximum power point). For aerogel films thicker than 6 μm, J_{sc} and power conversion efficiencies increase only marginally, even though light-harvesting efficiencies are enhanced with increasing photoanode thickness (Table 2). From these observations, it is clear that, even for aerogel electrodes of 8 μm thickness, charge recombination events already compromise charge-collection efficiencies. At the same time, as the electrode thickness increases from ca. 6 μm to ca. 14 μm, the DSC dark current systematically increases (see Supporting Information, Figure S2). Consequently, as the photoelectrode becomes thicker (and J_{sc} very slightly increases), the values for V_{oc} and the fill factor decrease slightly. The end result is that the overall power conversion efficiency remains unchanged for photoanodes

dx.doi.org/10.1021/jp112139h |J. Phys. Chem. C XXXX, XXX, 000–000

Table 2. Performances of Ni(III)/(IV) Bis(dicarbollide) DSCs Employing Nanoparticle and Aerogel Frameworks of Various Thicknesses with No ALD Al_2O_3 Modification[a]

framework	film thickness (μm)	V_{oc} (mV)	J_{sc} (mA/cm^2)	FF (%)	efficiency (%)
nanoparticle	8.1	568	2.4	59	0.8
aerogel	5.8	628	5.3	65	2.1
aerogel	8.4	590	5.5	60	2.0
aerogel	13.6	586	6.3	56	2.1

[a] The SiO_2 aerogel films were conformally coated with 10.5 nm of TiO_2 by ALD.

in the 6−14 μm thickness range. These results are in reasonably good agreement with the modeling-based predictions for a maximum diffusion length, L_n, of around 20 μm.[34]

The progressive decrease in V_{oc} beyond 6 μm further supports the conclusion that, for thicker electrodes, the aerogel DSCs are limited by charge recombination through the TiO_2 frameworks. In contrast to I^-/I_3^--containing cells, where charge collection is already highly efficient even for 10−15 μm thick electrodes, improvements (higher photocurrent densities) in the nickel-based metallacarborane system would be expected for thicker electrode materials featuring faster electron transport (e.g., ZnO electrodes in place of TiO_2),[35] which would translate to significantly longer charge-collection distances. Alternatively, or additionally, the performance of Ni(III)/(IV) bis(dicarbollide) based cells would likely be enhanced by using more strongly absorbing chromophores.[36] We intend to report shortly on studies with alternative chromophores. Additionally, it will be important to determine the long-term stability of the shuttle under cell operating conditions. On account of the comparatively short (and presumably strong) nickel−carbon bonds for both forms of the bis(dicarbollide) complex,[37] we are optimistic that the shuttle will prove to be chemically stable; however, the problem requires experimental investigation.

CONCLUSIONS

Rigid, TiO_2-ALD-modified, aerogel thin films were successfully introduced into DSCs that utilize the Ni(III)/(IV) bis(dicarbollide) redox shuttle. These porous, high-surface-area photoanodes give enhanced photocurrents: over 6 mA/cm^2 under AM 1.5 conditions, compared to only 2.4 mA/cm^2 with photoanodes based on nanoparticles. The ease of tailorability of the aerogel framework, in terms of porosity and shell dimensions in SiO_2@TiO_2 structures, should make them attractive for other DSCs employing unconventional shuttles, especially in cases where slow diffusion of the shuttle otherwise limits DSC performance.

Through electrochemical impedance spectroscopic analysis, we find that electron transport is faster in the aerogel structure—behavior that would be expected if the conduction band edge is lower for the aerogel material relative to the nanoparticulate material. At the same time, we find that recombination rates at identical cell potentials (for example, the open-circuit potential) are more or less identical. The combination of the two effects yields a greater charge-collection length at a given cell potential (such as the maximum power point or at short circuit), resulting in greater photocurrent density for the aerogel-based device. Somewhat surprising, in view of the apparent difference in conduction band edge energy, are the identical rates of recombination. All else being equal, one would expect recombination to be much slower at the nanoparticle/solution interface than at the aerogel/solution interface (because of the greater difference between the conduction band edge and the quasi-Fermi level for the latter). That the recombination rates are not slower is likely a consequence of additional recombination at the nanoparticle/solution interface involving surface defect states. This explanation is supported by the finding that atomic layer deposition of submonolayer amounts of alumina, known to passivate trap states, has a significant inhibitory effect upon recombination at the nanoparticle/solution interface, but no effect[38] at the aerogel/solution interface. As a result, Ni metallacarborane containing DSCs that use aerogel photoelectrodes exhibit substantially higher photocurrent densities and power conversion efficiencies than do Ni metallacarborane containing DSCs that use nanoparticulate photoelectrodes. The use of such open (aerogel) frameworks may also enable the use of dye molecules that are too large to be accommodated by nanoparticle-based electrodes.

ASSOCIATED CONTENT

Supporting Information. Krypton-based adsorption isotherm measurements, roughness factor calculations for TiO_2@SiO_2 aerogel thin films, and dark $J-V$ curves for aerogel-based DSCs with varying photoanode thickness. This material is available free of charge via the Internet at http://pubs.acs.org.

AUTHOR INFORMATION

Corresponding Author

*E-mail: j-hupp@northwestern.edu (J.T.H.); t-marks@northwestern.edu (T.J.M.); chadnano@northwestern.edu (C.A.M.); fran.fabregat@fca.uji.es (F.F.-S.).

ACKNOWLEDGMENT

J.T.H. and T.J.M. gratefully acknowledge the support of BP Solar. J.T.H. thanks the U.S. DOE Office of Science (Grant DE-FG02-87ER13808). O.K.F. thanks NU-NSEC for partial support. T.J.M. also acknowledges the support of the Energy Frontier Research Center (DE-SC0001059) at the ANSER Center of Northwestern University. C.A.M. acknowledges the DOE Office of Science (Award No. DE-SC0000989) for support via the NU Nonequilibrium Energy Research Center. C.A.M. is also grateful for support from the U.S. ARO. J.B., F.F.-S. and S.R.R. thank Generalitat Valenciana under Project PROMETEO/2009/058 and Ministerio de Ciencia e Innovación under Projects HOPE CSD2007-00007 and MAT2010-19827 for financial support.

REFERENCES

(1) Hamann, T. W.; Jensen, R. A.; Martinson, A. B. F.; Ryswyk, H. V.; Hupp, J. T. *Energy Environ. Sci.* **2008**, *1*, 66–78.

(2) (a) O'Regan, B.; Grätzel, M. *Nature* **1991**, *353*, 737. (b) Grätzel, M. *Inorg. Chem.* **2005**, *44*, 6841.

(3) (a) Nusbaumer, H.; Moser, J.-E.; Zakeeruddin, S. M.; Nazeeruddin, M. K.; Grätzel, M. *J. Phys. Chem. B* **2001**, *105*, 10461–10464. (b) Nelson, J. J.; Amick, T. J.; Elliott, C. M. *J. Phys. Chem. C* **2008**, *112*, 18255–18263. (c) Moon, S.-J.; Yum, J.-H.; Humphry-Baker, R.; Karlsson, K. M.; Hagberg, D. P.; Marinado, T.; Hagfeldt, A.; Sung, L.; Grätzel, M.; Nazeeruddin, M. K. *J. Phys. Chem. C* **2009**, *113*, 16816–16820.

(4) Martinson, A. B. F.; Hamann, T. W.; Pellin, M. J.; Hupp, J. T. H. *Chem.—Eur. J.* **2008**, *14*, 4458–4467.

(5) Snaith, H. J. *Adv. Funct. Mater.* **2010**, *20*, 13–19.
(6) Boschloo, G.; Hagfeldt, A. *Acc. Chem. Res.* **2009**, *42*, 1819–1826.
(7) Marton, A.; Clark, C. C.; Srinivasan, R.; Freundlich, R. E.; Sarjeant, A. A. N.; Meyer, G. J. *Inorg. Chem.* **2006**, *45*, 362–369.
(8) Gardner, J. M.; Abrahamsson, M.; Farnum, B. H.; Meyer, G. J. *J. Am. Chem. Soc.* **2009**, *131*, 16206–16214.
(9) Splan, K. E.; Massari, A. M.; Hupp, J. T. *J. Phys. Chem. B* **2004**, *108*, 4111–4115.
(10) Clark, C. C.; Marton, A.; Srinivasan, R.; Sarjeant, A. A. N.; Meyer, G. J. *Inorg. Chem.* **2006**, *45*, 4728–4734.
(11) O'Regan, B. C.; Lopez-Duarte, I.; Martinez-Diaz, M. V.; Forneli, A.; Albero, J.; Morandeira, A.; Palomares, E.; Torres, T.; Durrant, J. R. *J. Am. Chem. Soc.* **2008**, *130*, 2906–2907.
(12) (a) Li, T. C.; Spokoyny, A. M.; She, C.; Farha, O. K.; Mirkin, C. A.; Marks, T. J.; Hupp, J. T. *J. Am. Chem. Soc.* **2010**, *132*, 4580–4582. (b) Hamann, T. W.; Farha, O. K.; Hupp, J. T. *J. Phys. Chem. C* **2008**, *112*, 19756–19764.
(13) Hawthorne, M. F.; Zink, J. I.; Skelton, J. M.; Bayer, M. J.; Liu, C.; Livshits, E.; Baer, R.; Neuhauser, D. *Science* **2004**, *303*, 1849–1851.
(14) (a) Spokoyny, A. M.; Li, T. C.; Farha, O. K.; Machan, C. W.; She, C.; Stern, C. L.; Marks, T. J.; Hupp, J. T.; Mirkin, C. A. *Angew. Chem., Int. Ed.* **2010**, *49*, 5339–5343. (b) González-Cardoso, P.; Stoica, A.-I.; Farràs, P.; Pepiol, A.; Viñas, C.; Teixidor, F. *Chem.—Eur. J.* **2010**, *16*, 6660–6665.
(15) (a) Qian, J.; Liu, P.; Xiao, Y.; Jiang, Y.; Cao, Y.; Ai, X.; Yang, H. *Adv. Mater. (Weinheim, Germany)* **2009**, *21*, 1–5. (b) Yang, S.-C.; Yang, D.-J.; Kim, J.; Hong, J.-M.; Kim, H.-G.; Kim, I.-D.; Lee, H. *Adv. Mater. (Weinheim, Germany)* **2008**, *20*, 1059–1064. (c) Koo, H.-J.; Kim, Y. J.; Lee, Y. H.; Lee, W. I.; Kim, K.; Park, N.-G. *Adv. Mater. (Weinheim, Germany)* **2008**, *20*, 195–199.
(16) (a) Gong, D.; Grimes, C. A.; Varghese, O. K.; Hu, W.; Singh, R. S.; Chen, Z.; Dickey, E. C. *J. Mater. Res.* **2001**, *16*, 3331. (b) Martinson, A. B. F.; Elam, J. W.; Hupp, J. T.; Pellin, M. J. *Nano Lett.* **2007**, *7*, 2183–2187. (c) Kang, T.-S.; Smith, A. P.; Taylor, B. E.; Durstock, M. F. *Nano Lett.* **2009**, *9*, 601–606. (d) Kim, D.; Ghicov, A.; Albu, S. P.; Schmuki, P. *J. Am. Chem. Soc.* **2008**, *130*, 16454–16455.
(17) Hamann, T. W.; Martinson, A. B. F.; Elam, J. W.; Pellin, M. J.; Hupp, J. T. *J. Phys. Chem. C* **2008**, *112*, 10303–10307.
(18) Tillotson, T. M.; Hrubesh, L. W. *J. Non-Cryst. Solids* **1992**, *145*, 44–50.
(19) (a) Keis, K.; Magnusson, E.; Lindström, H.; Lindquist, S.-E.; Hagfeldt, A. *Sol. Energy Mater. Sol. Cells* **2002**, *73*, 51–58. (b) Gibson, E. A.; Smeigh, A. L.; Pleux, L. L.; Fortage, J.; Boschloo, G.; Blart, E.; Pellegrin, Y.; Odobel, F.; Hagfeldt, A.; Hammarström, L. *Angew. Chem., Int. Ed.* **2009**, *48*, 4402–4405. (c) Dabestani, R.; Bard, A. J.; Campion, A.; Fox, M. A.; Mallouk, T. E.; Webber, S. E.; White, J. M. *J. Phys. Chem.* **1988**, *92*, 1872–1878.
(20) Hamann, T. W.; Martinson, A. B. F.; Elam, J. W.; Pellin, M. J.; Hupp, J. T. *Adv. Mater. (Weinheim, Germany)* **2008**, *20*, 1560–1564.
(21) Rouquerol, F.; Rouquerol, J.; Sing, K. *Adsorption by Powders and Porous Solids. Principles, Methodology and Applications*; Academic Press: London, 1999.
(22) Krishtalik, L. I.; Alpatova, N. M.; Ovsyannikova, E. V. *Electrochim. Acta* **1991**, *36*, 435.
(23) Bisquert, J.; Fabregat-Santiago, F. Impedance spectroscopy: A general introduction and application to dye-sensitized solar cells. In *Dye-Sensitized Solar Cells*; Kalyanasundaram, K. Ed.; CRC Press: Boca Raton, FL, USA, 2010; ISBN: 978-2-940222-36-0.
(24) Note that the concentrations of the two candidate regenerators differ as well: $[Ni(IV)] = 1.8 \times 10^{-3}$ M and $[I_3^-] = 3.0 \times 10^{-2}$ M. Combining this information with the observed 100-fold difference in interception rate and assuming essentially identical reaction orders for the electron, we find that the ratio of rate *constants* for electron interception by Ni(IV) versus I_3^- is ~1700.
(25) (a) Bisquert, J. *Phys. Chem. Chem. Phys.* **2003**, *5*, 5360. (b) Barea, E. M.; Ortiz, J.; Payá, F. J.; Fernández-Lázaro, F.; Fabregat-Santiago, F.; Sastre-Santos, A.; Bisquert, J. *Energy Environ. Sci.* **2010**, *3*, 1985–1994.
(26) (a) van de Lagemaat, J.; Park, N.-G.; Frank, A. J. *J. Phys. Chem. B* **2000**, *104*, 2044–2053. (b) Zhang, C.; Huo, Z.; Huang, Y.; Guo, L.; Sui, Y.; Hu, L.; Kong, F.; Pan, X.; Dai, S.; Wang, K. *J. Electroanal. Chem.* **2009**, *632*, 133–138.
(27) Fabregat-Santiago, F.; Bisquert, J.; Palomares, E.; Otero, L.; Kuang, D.; Zakeeruddin, S. M.; Grätzel, M. *J. Phys. Chem. C* **2007**, *111*, 6550–6560.
(28) The ca. 30-fold differences in conductivity for the aerogel versus the nanoparticle electrodes seem to demand an explanation. One possibility is that electron mobilities in the two types of TiO_2 (anatase) differ greatly; another is that doping densities differ greatly. Neither explanation seems fully satisfying, as the mobilities or conductivities would need to differ by ca. 2 orders of magnitude. A third possibility is that the value of E_C is lowered by 0.25 V upon replacement of the nanoparticle structure by the aerogel electrode. While we do not have a compelling explanation for the shift in band-edge energy, we speculate that this is the primary explanation. With this in mind, we have "corrected" the nanoparticle-derived data in Figure 8 for the putative band-edge energy difference; see Figure 9.
(29) The underlying assumptions in shifting E_C is that at a given potential below the band edge the conductivities for the two forms of titanium dioxide should be similar or identical. In other words, conductivity is achieved mainly by thermally promoting electrons to the conduction band, rather than by having electrons hop, for example, from trap site to trap site without sampling the conduction band.
(30) Fabregat-Santiago, F.; Bisquert, J.; Cevey, L.; Chen, P.; Wang, M.; Zakeeruddin, S. M.; Grätzel, M. *J. Am. Chem. Soc.* **2009**, *131*, 558–562.
(31) Since trapping by, and charge transfer from, surface states or band-gap-localized states near the particle surface, is known to contribute to recombination events in conventional DSCs, passivation of these states in the nanoparticle case was done via ALD of an ultrathin layer of Al_2O_3 (i.e. one cycle, corresponding to about half a monolayer). (See, for example: Li, T. C. *J. Phys. Chem. C* **2009**, *113*, 18385–18390 and ref 6.) In the absence of the passivation process, the disparity in charge-collection lengths for aerogel versus nanoparticle electrodes would likely be even greater.
(32) (a) Jennings, J. R.; Peter, L. M. *J. Phys. Chem. C* **2007**, *111*, 16100. (b) Quitana, M.; Edvinsson, T.; Hagfeldt, A.; Boschloo, G. *J. Phys. Chem. C* **2007**, *111*, 1035–1041. (c) Fabregat-Santiago, F.; Bisquert, J.; Cevey, L.; Chen, P.; Wang, M.; Zakeeruddin, S. M.; Grätzel, M. *J. Am. Chem. Soc.* **2009**, *131*, 558–562.
(33) (a) Bisquert, J.; Mora-Seró, I. *J. Phys. Chem. Lett.* **2010**, *1*, 450–456. (b) Jennings, J. R.; Li, F.; Wang, Q. *J. Phys.Chem. C* **2010**, *114*, 14665–14674.
(34) An alternative approach to estimating the approximate thickness of the useful portion (i.e., significantly photocurrent-contributing portion) of the photoelectrode is to examine the IPCE data. From N719 dye desorption of an 8 μm thick TiO_2 photoanode, the light-harvesting efficiency ($LHE = 1 - 10^{-Absorbance}$) was calculated to be 76%. By artificially attenuating the dye absorption to match the LHE to that derived from the aerogel DSC IPCE, it is estimated that 100% charge collection occurs through 2 μm, assuming 100% charge injection. However, unpublished results with this Ni(III)/(IV) bis(dicarbollide) system indicate that injection decreases ~50% using an electrolyte with no Li^+ and only base as an additive. Therefore, although reflective losses and light scattering are not taken into account, it is reasonable to estimate that contributions to the photocurrent are dominated by electrons injected within the first 4 μm of the electrode. This, in turn, suggests that L_n is approximately 12 μm. In view of the approximate nature of the IPCE-based analysis, this result can be considered to be in reasonably good agreement with the value of 20 μm derived from impedance spectroscopy.
(35) Martinson, A. B. F.; Góes, M. S.; Fabregat-Santiago, F.; Bisquert, J.; Pellin, M. J.; Hupp, J. T. *J. Phys. Chem. A* **2009**, *113*, 4015–4021.
(36) (a) Dy, J. T.; Tamaki, K.; Sanehira, Y.; Nakazaki, J.; Uchida, S.; Kubo, T.; Segawa, H. *Electrochemistry* **2009**, *77*, 206–209. (b) Robson, K. C. D.; Koivisto, B. D.; Gordon, T. J.; Baumgartner, T.; Berlinguette, C. P. *Inorg. Chem.* **2010**, *49*, 5335–5337.
(37) Hurvois, J. P.; Moinet, C. *J. Organomet. Chem.* **2005**, *690*, 1829–1839.
(38) Li, T. C. Unpublished results.